JOURNAL OF SYNCHROTRON RADIATION

ISSN 1600-5775

Phase-contrast 3D tomography of HeLa cells grown in PLLA polymer electrospun scaffolds using synchrotron X-rays

A. Bhartiya,[a,b] K. Madi,[c] C. M. Disney,[d] L. Courtois,[c] A. Jupe,[e] F. Zhang,[a,b,f] A. J. Bodey,[g] P. Lee,[h] C. Rau,[g] I. K. Robinson[a,b,i] and M. Yusuf[a,b,j]*‡

[a]London Centre for Nanotechnology, University College London, London WC1H 0AH, UK, [b]Research Complex at Harwell Rutherford Appleton Laboratory, Didcot OX11 0FA, UK, [c]3DMagination Ltd, Atlas Building, Fermi Avenue, Harwell, Didcot OX11 0QX, UK, [d]School of Mechanical, Aerospace and Civil Engineering, University of Manchester, Manchester, UK, [e]Department of Applied Computing, The University of Buckingham, UK, [f]Department of Electrical and Electronic Engineering, Southern University of Science and Technology, Shenzhen 518055, People's Republic of China, [g]Diamond Light Source, Oxfordshire OX11 0DE, UK, [h]Mechanical Engineering, University College London, London WC1E 7JE, UK, [i]Condensed Matter Physics and Materials Department, Brookhaven National Laboratory, Upton, NY 11973, UK, and [j]Centre for Regenerative Medicine and Stem Cell Research, Aga Khan University, Karachi, Pakistan. *Correspondence e-mail: ucanymo@ucl.ac.uk

Received 9 July 2019
Accepted 18 November 2019

Edited by R. W. Strange, University of Essex, UK

‡ Alternative e-mail address: mohammed.yusuf@aku.edu

Keywords: 3D culture; electrospun polymer scaffold; X-ray CT; synchrotron; image analysis; *Avizo*.

Supporting information: this article has supporting information at journals.iucr.org/s

Advanced imaging is useful for understanding the three-dimensional (3D) growth of cells. X-ray tomography serves as a powerful noninvasive, nondestructive technique that can fulfill these purposes by providing information about cell growth within 3D platforms. There are a limited number of studies taking advantage of synchrotron X-rays, which provides a large field of view and suitable resolution to image cells within specific biomaterials. In this study, X-ray synchrotron radiation microtomography at Diamond Light Source and advanced image processing were used to investigate cellular infiltration of HeLa cells within poly L-lactide (PLLA) scaffolds. This study demonstrates that synchrotron X-rays using phase contrast is a useful method to understand the 3D growth of cells in PLLA electrospun scaffolds. Two different fiber diameter (2 and 4 µm) scaffolds with different pore sizes, grown over 2, 5 and 8 days *in vitro*, were examined for infiltration and cell connectivity. After performing visualization by segmentation of the cells from the fibers, the results clearly show deeper cell growth and higher cellular interconnectivity in the 4 µm fiber diameter scaffold. This indicates the potential for using such 3D technology to study cell–scaffold interactions for future medical use.

1. Introduction

Tissue engineering is an expanding interdisciplinary field combining life, material and bioengineering sciences, aiming to restore damaged tissue and organs (Langer & Vacanti, 1993; Gurtner *et al.*, 2007). The goal is to produce a three-dimensional (3D) construct(s) that uses live cells supported by a scaffold that replicates *in vivo* conditions for successful tissue/organ replacement. These 3D scaffolds provide support and allow cellular growth processes, such as cell adhesion, migration, proliferation and differentiation, to take place (Bružauskaitė *et al.*, 2016; Fletcher & Mullins, 2010), maintaining tissue homeostasis *in vitro* (Lenas *et al.*, 2009). Scaffolds serve as suitable models for cell growth in which *in vitro* cancer cell behavior can be investigated (Rijal *et al.*, 2017; Rijal & Li, 2017; Fischbach *et al.*, 2007). Before designing any experiment, the type and design of the scaffold, growth factors, the extracellular matrix (ECM) and cells of choice (Zhang, 2008) need to be selected carefully for the required application.

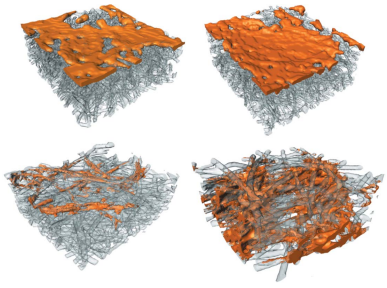

A number of different biomaterials have been developed for tissue engineering applications. This includes both naturally derived and synthetic polymers (Bhattarai *et al.*, 2018). Using electrospinning technology, highly porous scaffolds with interconnected pores or random fiber networks can be produced (Pan & Ding, 2012; Lannutti *et al.*, 2007). Materials for scaffolds include poly(L-lactic acid) (PLLA) that has received approval from US Food and Drug Administration (FDA) for human clinical use (Ma, 2004; Thomson *et al.*, 1995), making it a material of interest. Furthermore it can be easily processed, can degrade to natural metabolites, and has mechanical properties that can be adjusted to specific requirements (Lin *et al.*, 2006). The scaffold fiber diameter can range from the nanoscale to the microscale (Bradley *et al.*, 2017; Subbiah *et al.*, 2005; Li *et al.*, 2002) and should ideally resemble the ECM dimensions.

To understand scaffold characteristics such as architecture, cell infiltration and growth of cells, imaging serves as a useful tool (Sengers *et al.*, 2007). As scaffolds can have a varied structure in the depth dimension, certain characteristics are not observable using standard 2D imaging methods. For example, scanning electron microscopy (SEM) has been routinely used to image the surface of scaffolds seeded with cells (Millas *et al.*, 2014; Yusuf *et al.*, 2014).

The microscopy technique used depends on the thickness of the scaffold. Imaging of cells grown in scaffolds using standard light microscopy poses several problems as the 3D structure cannot be fully characterized mainly due to the thickness of the scaffold and the light diffracting (Graf & Boppart, 2010). Confocal imaging of fluorescent labeled live cells has a greater depth up to 350 µm but can vary depending on properties of the sample (Cox & Sheppard, 2004; Boustany *et al.*, 2010). Higher resolution can be obtained using multiphoton fluorescence microscopy that allows simultaneous excitation at multiple long wavelengths (Georgakoudi *et al.*, 2008). These techniques are useful but require fluorescent labeling of the sample giving sparse information. Furthermore, high light intensities often lead to fluorophore bleaching and phototoxic effects (Pampaloni *et al.*, 2007). Both fluorescence and confocal microscopy cannot see the interior of the 'opaque' scaffold. To overcome this, 3D rendering of sections imaged using confocal microscopy after cryofixing fluorescent cells has been carried out (Roy *et al.*, 2009). However, obtaining 2D sections and performing 3D reconstructions either by confocal (Thevenot *et al.*, 2008) or focused ion beam (FIB-SEM) (Stachewicz *et al.*, 2015) is disruptive, tedious and can be destructive due to sectioning and/or staining processes. It is clear that new imaging approaches for tissue engineering applications need to be further explored and developed (Appel *et al.*, 2014).

Nondestructive 3D imaging at high resolution can be achieved using X-ray tomography (Bradley & Withers, 2016) of large samples (up to a few cm^3 in size) with high resolution (submicrometre), and allows quantitative measurements (du Plessis *et al.*, 2017). Microcomputed tomography (microCT) has been used widely for biological sample imaging and allows deep penetration into the sample (du Plessis *et al.*, 2017; Mizutani & Suzuki, 2012). The method uses 2D X-ray images at different angles around the sample (usually 180° or 360°). After 3D reconstruction, sophisticated analysis can be carried out using different software tools (Kalender, 2006). This technology has been used for imaging scaffolds containing cells using laboratory-based X-ray systems by phase contrast (Pan & Ding, 2012; Shepherd *et al.*, 2018; Dorsey *et al.*, 2009). Even though the X-rays can penetrate through the sample and provide high resolution (150 nm), the main disadvantage is the limited field of view (Bradley *et al.*, 2017). Better phase contrast can be achieved using microCT systems generated in a synchrotron to image cells, as a synchrotron source generates high spatial coherence and high flux (Zehbe *et al.*, 2014). In addition, the use of heavy metal staining can be eliminated when performing phase-contrast imaging which is advantageous to keep structural details intact (Giuliani *et al.*, 2018).

In this study, non-toxic and FDA-approved electrospun PLLA scaffolds were used. Our study assessed and compared two different fiber diameter scaffolds. An immortal HeLa cancer cell line was selected as it is the most widely used model cell line that has contributed towards many medical science discoveries. These cells grow fast with a doubling time of 24 h, making them ideal for developing protocols (Hyman & Simons, 2011). This paper demonstrates the use of synchrotron X-ray microCT for imaging cells grown in electrospun PLLA scaffolds giving a large field of view. Also, the effect of different scaffold fiber/pore sizes on cancer cell growth and infiltration was tested. Unstained cells were seeded and measured at three different time points in two different fiber/pore-sized scaffolds.

2. Material and method

2.1. Sample preparation

The scaffold material was purchased from the Electrospinning Company, UK (https://www.electrospinning.co.uk/). The electrospun scaffolds used were made of PLLA and have 2 µm- and 4 µm-diameter fibers with random orientations. The pore sizes are 14.8 ± 4.3 µm and 22.7 ± 8.1 µm for the 2 µm- and 4 µm-diameter fiber scaffolds, respectively. The Electrospinning Company, that produced and manufactured these scaffolds, had already carried out fiber distribution analysis [carried out using Phenom World (SEM) with FiberMetric software] on the products used as part of their routine analysis and quality control. This information is listed on their website https://www.electrospinning.co.uk/services/bespoke-scaffolds/. The fibers are randomly orientated and the fiber distribution analysis shows less than 10% dispersity in the fiber diameters, and the standard deviation around the mean is less than 15%. The scaffolds were in the form of 2 cm-diameter disks with a thickness of around 50 µm. HeLa cells were obtained from Professor Stanley Botchway (Central Laser Facility, Science and Technology Facilities Council, UK). These cells were grown in the scaffold material following previously published protocols (Bradley *et al.*, 2017; Yusuf *et al.*, 2014). Briefly, HeLa cells were grown in electrospun porous PLLA scaffolds

for 2, 5 and 8 days. The scaffolds containing cells were then fixed using 2.5% (vol/vol) glutaraldehyde (Sigma Aldrich, UK) in 0.1 *M* cacodylate buffer (Sigma Aldrich, UK) (pH 7.2) for 2 h. Afterwards, the samples were washed three times with 0.1 *M* cacodylate buffer (pH 7.2), followed by dehydration using a series of ethanol solutions (70%, 85% and 100%). The samples were finally dried at room temperature using hexamethyldisilazane (Sigma-Aldrich, UK) for 5 min. Before X-ray scanning, scaffolds were prepared into thin strips by cutting the scaffold material using a sharp blade or scissors. Once the strips were made, the scaffold material was carefully placed within 1.8 mm-diameter kapton tubing (Goodfellow, UK) ensuring there were no folds. Mounting of the sample in the kapton tubing for the microCT was done as described previously (Bradley *et al.*, 2017) by gluing the kapton tubing onto a pin holder that then attached onto the rotation stage.

2.2. Beamline I13-2 at Diamond Light Source for X-ray tomography

In-line phase-contrast microtomography was performed using the Diamond–Manchester Imaging Branchline I13-2 of the third-generation synchrotron Diamond Light Source (DLS). Traditionally, monochromatic X-rays have been used for phase-contrast-enhanced images; instead, we used a pink beam (5–35 keV) to enable similar data quality with shorter acquisition times (Rau *et al.*, 2011, 2016; Pešić *et al.*, 2013). Tomography scans using the pco.edge 5.5 detector at 8× total magnification was performed. The field of view was 2.1 mm × 1.8 mm with an effective pixel size of 0.81 µm. The high flux of the X-ray beam allowed tomography datasets to be recorded rapidly. The exposure time was set to 20 ms per radiograph with a 0.045° step size, obtaining 4001 projections per data set. A filtered back-projection algorithm with dark- and flat-field correction reconstructed 3D volumes from the projections using DLS software *DAWN* (Basham *et al.*, 2015).

2.3. Data analysis

Data were analyzed using powerful dedicated graphic workstations at I13-2 (DLS) (Rau *et al.*, 2016; Basham *et al.*, 2015). After reconstruction, the 3D datasets were converted from 32-bit tiff images into 8-bit images using *ImageJ/Fiji* software. The kapton tubing artifacts that were seen around the scaffold material were cropped out, reducing the size of the data. A region of interest was created from the full data set that had dimensions of 722 × 522 × 667 voxels. A 2D slice or plane in *XZ* was aligned with the surface and used to determine visually the apparent growth of cells within the scaffold as a first inspection. This was done for all the 2 µm and 4 µm fiber diameter scaffold samples and for different numbers of days (2, 5 and 8 days).

2.4. Image processing

Image processing was performed using Thermo Scientific *Amira-Avizo* 9.5 software. The 3D datasets were filtered using a non-local means algorithm to de-noise the images while preserving the boundaries between the scaffold fibers and the cells. The scaffold and the cells were separately segmented using a 3D-region growing algorithm. A Euclidean distance map was computed from a binary mask that included both scaffold fibers and pores. A Python script was then developed to quantify the volume of cells as a function of the distance from the two opposite scaffold edges. At a given depth, the volume fraction of cells, defined as the volume of cells divided by the volume of both fibers and pores, was also calculated. The script was adjusted to quantify the volume of the cells from the upper scaffold surface where the cells have grown.

3. Results and discussion

The X-ray scans gave a large field of view (2.1 mm × 1.8 mm) with cells clearly visible on the surface of the scaffold after aligning the tomograms [Fig. 1(*a*)].

Obtaining a large field of view is important as cells can grow in different orientations according to the scaffold architecture. The subvolumes show a clear distribution of cells on the seeded surface with reduced contrast difference between the scaffold and cells observed for all the samples used in the study. Fig. 1(*b*) and Figs. S1(A)–S1(F) of the supporting information show tomograms of 2 µm and 4 µm fiber diameter scaffolds with cells grown for different durations (2, 5 and 8 days). To visualize cell distribution within the two scaffold types (2 µm and 4 µm fiber diameter) over the different days (2, 5 and 8 days), the volume fraction of cells as a function of the distance from the scaffold surface was measured. For the 4 µm fiber diameter scaffold, the duration of 2 days was not included as there were very few cells to segment, so was excluded from the analysis [Fig. S1(D) of the supporting information]. Fig. 2(*a*) shows that cells in the 2 µm fiber diameter scaffold migrate to a depth of approximately 10 µm after 2 days to 16 µm after 5 days and 15.2 µm after 8 days. In comparison, cells in the 4 µm fiber diameter scaffold showed a depth of 43.2 µm and 48.8 µm after 8 days [Fig. 2(*b*)]. Connected cells in the entire scaffold have been displayed in 3D using different colors to identify clusters [Figs. 2(*c*) and 2(*d*), and Figs. S2(A)–S2(C) of the supporting information]. The 4 µm fiber diameter scaffold at 8 days has one color (in blue) because all the cells are interconnected [Fig. 2(*d*)], whereas the other cells are clustered in multiple colors [Fig. 2(*c*) and Figs. S2(A)–S2(C) of the supporting information]. These clusters show that the cell density is increasing with the growth of cells from 2 days to 8 days. Fig. S3 of the supporting information shows cells on the surface of the 2 µm fiber diameter scaffold.

The reconstructed images of cells cultured on fibrous scaffolds showed that they can grow within both types of fibrous scaffolds used. Cells attached to the surface of the 2 µm fiber diameter scaffold were distributed mainly on the surface, whereas cells on the 4 µm fiber diameter scaffold were distributed both on the surface and within (*z*) (Fig. 3).

The 2 µm fiber diameter scaffold was not suitable for cell infiltration into the pores between and among fibers. However, if cells were left in the 2 µm-diameter scaffold for longer, they

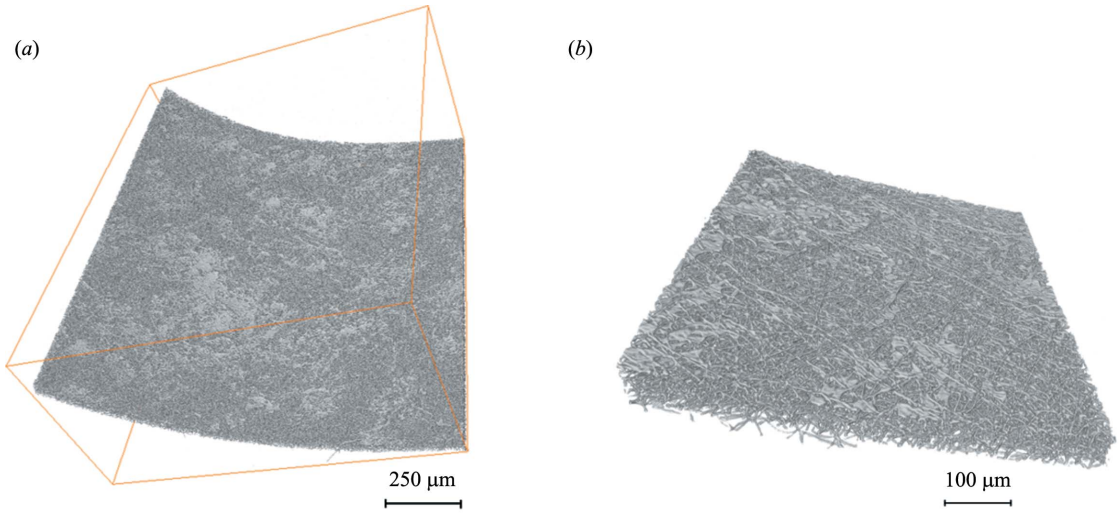

Figure 1
3D X-ray image of cells grown in electrospun scaffolds. (*a*) A full field of view, 2.1 mm × 1.8 mm, showing a 3D PLLA scaffold image with cells (white) distributed on the surface of the scaffold. Scale bar = 250 µm. (*b*) Subvolume of (*a*) showing an enlarged section with cellular detail on the surface of the scaffold visible including individual scaffold fibers. Scale bar = 100 µm.

may have migrated further inside the scaffold material. The 4 µm-diameter scaffold has a larger pore size (15–30 µm) than the 2 µm (5–10 µm) fiber scaffold. It is already known that the physical properties of the 3D matrix such as pore size, porosity and fiber diameter can affect cell morphology, attachment and function (Hollister, 2005; Causa *et al.*, 2007). The scaffold acts as a structural support and needs pores to allow cell attachment proliferation and migration. The cells should have access to oxygen and nutrients as well as be able to remove waste products (Lin *et al.*, 2006).

The use of X-ray tomography together with sophisticated 3D analysis has been demonstrated in recent studies investigating different polycaprolactone scaffolds for bone tissue regeneration (Shkarina *et al.*, 2018; Gorodzha *et al.*, 2017) and after checking the effect of the mineralization behavior of $CaCO_3$ deposited on such scaffolds followed by two plasma treatments (Ivanova *et al.*, 2018). It is evident that the future will involve using such methods not only for investigating scaffold characteristics but also combining detailed cell analysis investigating cell adhesion, growth, viability morphology and differentiation (Ivanova *et al.*, 2018). Nevertheless, X-ray microCT methodology is costly and involves gaining access to a synchrotron facility, but has advantages requiring no staining and high flux. As the large field of view comes at the cost of spatial resolution, precise analysis of nanofibers cannot be achieved (Shkarina *et al.*, 2018). We are also now witnessing 3D imaging studies moving towards cryo imaging of cells to understand scaffold–cell interactions. Cryo FIB-SEM has been used to evaluate cryo-prepared electrospun nanofibre scaffolds on which osteoblasts were grown (Urszula *et al.*, 2016). Even though cryo-imaging using soft X-ray cryo-microscopy of unstained cryo-fixed cells in the water window range have been imaged, it cannot be used to image

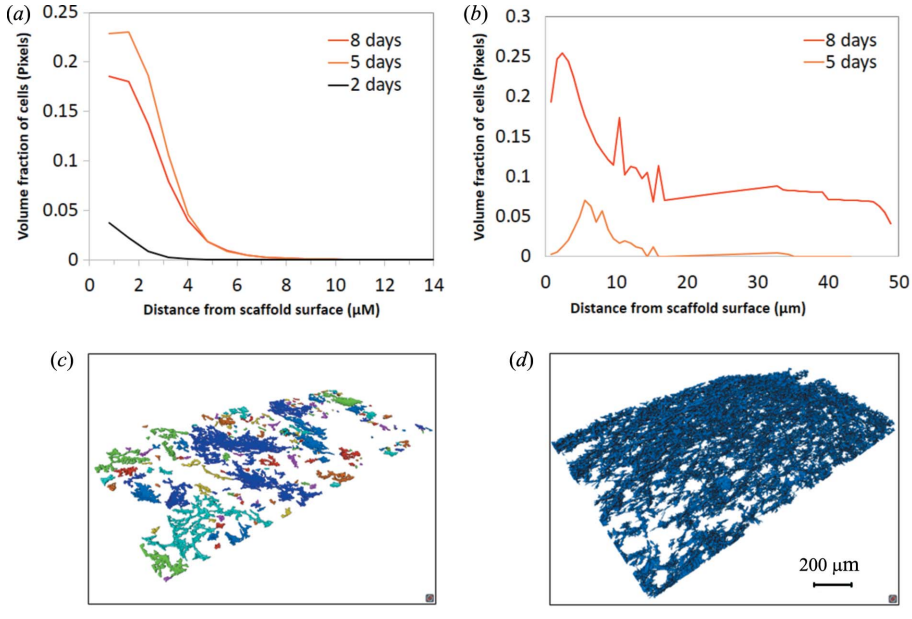

Figure 2
Volume fraction of cell voxels as a function of the distance from the scaffold surface. (*a*) Graph showing a comparison between cells grown for 2, 5 and 8 days for the 2 µm fiber diameter scaffold. (*b*) Graph showing a comparison between cells grown for 5 and 8 days for the 4 µm fiber diameter scaffold. (*c* and *d*) 3D visualization of the whole cells with each color denoting a group of cells that are connected: 8 days for the 2 µm fiber thick scaffold (*c*) and 8 days for the 4 µm fiber diameter scaffold (*d*). Scale bar = 200 µm.

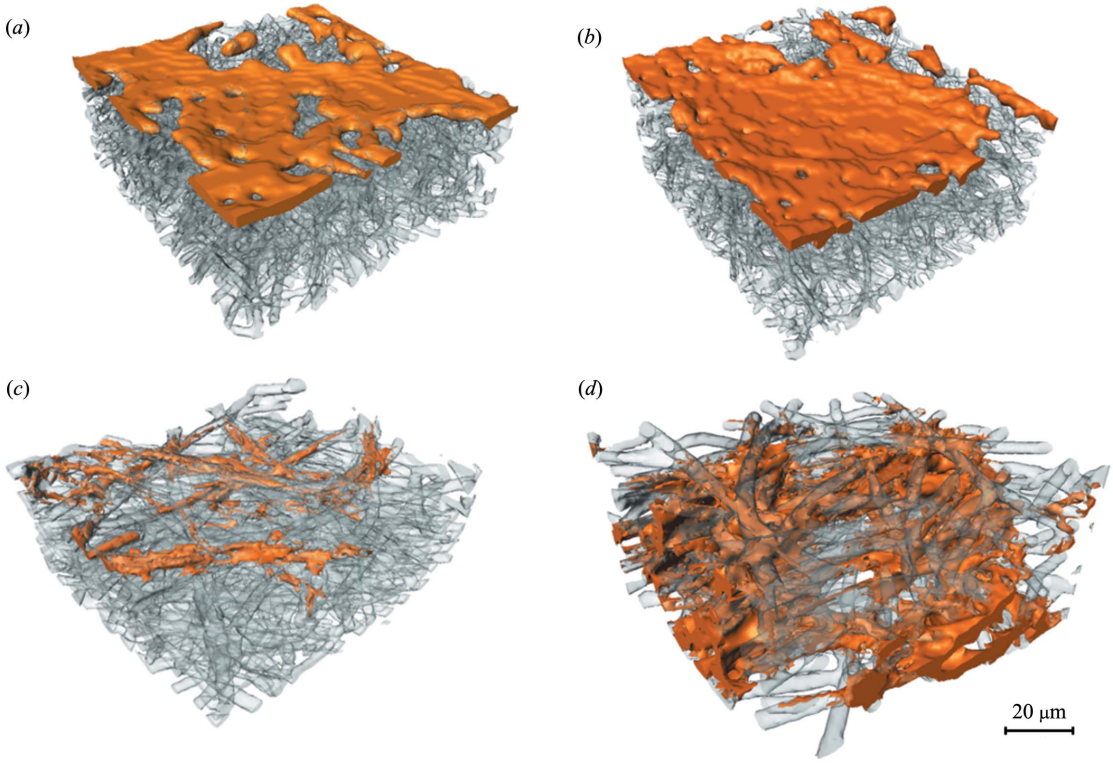

Figure 3
3D rendering of cells grown in electrospun scaffold material. Subvolume (130 μm) of 2 μm fiber diameter scaffold in gray and cells in orange after (*a*) 5 days and (*b*) 8 days of growth. Subvolume (130 μm) of the 4 μm fiber diameter scaffold in gray and cells in orange after (*c*) 5 days and (*d*) 8 days of growth. Scale bars for (*b*) and (*c*) are 20 μm.

scaffold–cells due to the thickness of the samples (Fogelqvist *et al.*, 2017).

4. Conclusion

Overall this study has demonstrated that X-ray microtomography with inline phase contrast serves as a suitable imaging method for the 3D observation of cells grown in electrospun scaffolds as it allows high penetration through the sample, is nondestructive and does not require any staining. The 3D scaffolds provide support to the cells and the cells show clear contact with one another. Clear segmentations can be performed in which cells can be separated from the scaffold, allowing us to understand the growth of cells within different scaffold types. Comparisons of the two scaffolds showed that HeLa cells in the 2 μm fiber diameter scaffold, with smaller pore sizes, did not penetrate into the material and formed cell sheets on the scaffold surface. Conversely, cells grown in the 4 μm scaffold fiber penetrated inside and grew within the scaffold. The results also show that cells are more interconnected in the 4 μm fiber diameters scaffold after 8 days of growth, penetrating throughout the entire 50 μm scaffold. This study will allow us to identify suitable platforms for cancer cell biology and metastasis, in which we will be able to understand the complex behavior of cells. Imaging the interior of scaffolds will also serve useful for other applications such as tissue and stem cell regeneration (Ivanova *et al.*, 2018).

Acknowledgements

The authors would like to thank the Electrospinning Company, Rutherford Appleton Laboratory, Harwell, Oxford, UK for regular discussion on scaffold material. The authors would also like to acknowledge the ongoing support of Professor El-Nasir MA Lalani of the Centre for Regenerative Medicine and Stem Cell Research at the Aga Khan University, Karachi. The authors would like to thank Professor Stanley Botchway (Central Laser Facility, Science and Technology Facilities Council, UK) for providing cells. Thanks also to Ms Safana Farooq and Ms Atiqa Sajid for proof-reading the manuscript.

Funding information

The following funding is acknowledged: Biotechnology and Biological Sciences Research Council (BBSRC, UK) (grant No. BB/H022597/1). IKR was partly supported by Brookhaven National Laboratory which is supported by the US Department of Energy, Office of Science, Office of Basic Energy Sciences, under Contract No. DE-SC0012704. CMD was supported by an EPSRC & MRC Centre for Doctoral Training (CDT) Regenerative Medicine (EP/L014904/1) studentship and EPSRC Doctoral Prize Fellowship (EP/R513131/1). FZ acknowledges funding from the National Natural Science Foundation of China (No. 11775105).

References

Appel, A. A., Anastasio, M. A., Larson, J. C. & Brey, E. M. (2014). *Biomaterials*, **71**, 3831–3840.

Basham, M., Filik, J., Wharmby, M. T., Chang, P. C. Y., El Kassaby, B., Gerring, M., Aishima, J., Levik, K., Pulford, B. C. A., Sikharulidze, I., Sneddon, D., Webber, M., Dhesi, S. S., Maccherozzi, F., Svensson, O., Brockhauser, S., Náray, G. & Ashton, A. W. (2015). *J. Synchrotron Rad.* **22**, 853–858.

Bhattarai, D. P., Aguilar, L. E., Park, C. H. & Kim, C. S. (2018). *Membranes*, **8**, 62.

Boustany, N. N., Boppart, S. A. & Backman, V. (2010). *Annu. Rev. Biomed. Eng.* **12**, 285–314.

Bradley, R. S., Robinson, I. K. & Yusuf, M. (2017). *Macromol. Biosci.* **17**, 1600236.

Bradley, R. S. & Withers, P. J. (2016). *MRS Bull.* **41**, 549–556.

Bružauskaitė, I., Bironaitė, D., Bagdonas, E. & Bernotienė, E. (2016). *Cytotechnology*, **68**, 355–369.

Causa, F., Netti, P. A. & Ambrosio, L. (2007). *Biomaterials*, **28**, 5093–5099.

Cox, G. & Sheppard, C. J. R. (2004). *Microsc. Res. Tech.* **63**, 18–22.

Dorsey, S. M., Lin-Gibson, S. & Simon, C. G. Jr (2009). *Biomaterials*, **30**, 2967–2974.

Fischbach, C., Chen, R., Matsumoto, T., Schmelzle, T., Brugge, J. S., Polverini, P. J. & Mooney, D. J. (2007). *Nat. Methods*, **4**, 855–860.

Fletcher, D. A. & Mullins, R. D. (2010). *Nature*, **463**, 485–492.

Fogelqvist, E., Kördel, M., Carannante, V., Önfelt, B. & Hertz, H. M. (2017). *Sci. Rep.* **7**, 13433.

Georgakoudi, I., Rice, W. L., Hronik-Tupaj, M. & Kaplan, D. L. (2008). *Tissue Eng. B*, **14**, 321–340.

Giuliani, A., Mencarelli, M., Frati, C., Savi, M., Lagrasta, C., Pompilio, G., Rossini, A. & Quaini, F. (2018). *Biomed. Phys. Eng. Expr.* **4**, 055008.

Gorodzha, S. N., Muslimov, A. R., Syromotina, D. S., Timin, A. S., Tcvetkov, N. Y., Lepik, K. V., Petrova, A. V., Surmeneva, M. A., Gorin, D. A., Sukhorukov, G. B. & Surmenev, R. A. (2017). *Colloids Surf. B Biointerfaces*, **160**, 48–59.

Graf, B. W. & Boppart, S. A. (2010). *Methods Mol. Biol.* **591**, 185–99.

Gurtner, G. C., Callaghan, M. J. & Longaker, M. T. (2007). *Annu. Rev. Med.* **58**, 299–312.

Hollister, S. J. (2005). *Nat. Mater.* **4**, 518–524.

Hyman, A. H. & Simons, K. (2011). *Nature*, **480**, 34.

Ivanova, A. A., Syromotina, D. S., Shkarina, S., Shkarin, R., Cecilia, A., Weinhardt, V., Baumbach, T., Saveleva, M. S., Gorin, D. A., Douglas, T. E. L., Parakhonskiy, B. V., Skirtach, A. G., Cools, P., De Geyter, N., Morent, R., Oehr, C., Surmeneva, M. A. & Surmenev, R. A. (2018). *RSC Adv.* **8**, 39106–39114.

Kalender, W. A. (2006). *Phys. Med. Biol.* **51**, R29–R43.

Langer, R. & Vacanti, J. P. (1993). *Tissue Eng. Sci.* **260**, 920–927.

Lannutti, J., Reneker, D., Ma, T., Tomasko, D. & Farson, D. (2007). *Mater. Sci. Eng. C*, **27**, 504–509.

Lenas, P., Moos, M. Jr & Luyten, F. P. (2009). *Tissue Eng. B*, **15**, 381–394.

Li, W.-J., Laurencin, C. T., Caterson, E. J., Tuan, R. S. & Ko, F. K. (2002). *J. Biomed. Mater. Res.* **60**, 613–621.

Lin, Y., Wang, L., Zhang, P., Wang, X., Chen, X., Jing, X. & Su, Z. (2006). *Acta Biomater.* **2**, 155–164.

Ma, P. X. (2004). *Mater. Today*, **7**, 30–40.

Millas, A. L. G., McKean, R., Stevens, R., Yusuf, M., Silveira, J. V. W., Puzzi, M. B. & Bittencourt, E. (2014). *Tissue Eng.* **4**, 217–220.

Mizutani, R. & Suzuki, Y. (2012). *Micron*, **43**, 104–115.

Pampaloni, F., Reynaud, E. G. & Stelzer, E. H. K. (2007). *Nat. Rev. Mol. Cell Biol.* **8**, 839–845.

Pan, Z. & Ding, J. (2012). *Interface Focus*, **2**, 366–377.

Pešić, Z, De Fanis, A., Wagner, U. & Rau, C. (2013). *J. Phys. Conf. Ser.* **425**, 182003.

Plessis, A. du, Broeckhoven, C., Guelpa, A. & le Roux, S. G. (2017). *Gigascience.* **6**, gix027.

Rau, C., Wagner, U., Pešić, Z. & De Fanis, A. (2011). *Phys. Status Solidi A*, **208**, 2522–2525.

Rau, C., Wagner, U. H., Vila-Comamala, J., Bodey, A., Parson, A., García-Fernández, M., De Fanis, A., Pešić, Z., Zanette, I. & Zdora, M. (2016). *AIP Conf. Proc.* **1741**, 030008.

Rijal, G., Bathula, C. & Li, W. (2017). *Int. J. Biomater.* **2017**, 8074890.

Rijal, G. & Li, W. (2017). *Sci. Adv.* **3**, e1700764.

Roy, D., Steyer, G. J., Gargesha, M., Stone, M. E. & Wilson, D. L. (2009). *Anat. Rec.* **292**, 342–351.

Sengers, B. G., Taylor, M., Please, C. P. & Oreffo, R. O. C. (2007). *Biomaterials*, **28**, 1926–1940.

Shepherd, D. V., Shepherd, J. H., Best, S. M. & Cameron, R. E. (2018). *J. Mater. Sci. Mater. Med.* **29**, 86.

Shkarina, S., Shkarin, R., Weinhardt, V., Melnik, E., Vacun, G., Kluger, P. J., Loza, K., Epple, M., Ivlev, S. I., Baumbach, T., Surmeneva, M. A. & Surmenev, R. A. (2018). *Sci. Rep.* **8**, 8907.

Stachewicz, U., Qiao, T., Rawlinson, S. C. F., Almeida, F. V., Li, W. Q., Cattell, M. & Barber, A. H. (2015). *Acta Biomater.* **27**, 88–100.

Subbiah, T., Bhat, G. S., Tock, R. W., Parameswaran, S. & Ramkumar, S. S. (2005). *J. Appl. Polym. Sci.* **96**, 557–569.

Thevenot, P., Nair, A., Dey, J., Yang, J. & Tang, L. (2008). *Tissue Eng. C*, **14**, 319–331.

Thomson, R. C., Wake, M. C., Yaszemski, M. J. & Mimkos, A. G. (1995). *Adv. Polym. Sci.* **122**, 245–274.

Urszula, S., Szewczyk, P., Kruk, A., Barber, A. & Czyrska-Filemonowicz, A. (2016). *Proceedings of the 16th European Microscopy Congress (EMC2016)*, 28 August–2 September 2016, Lyon, France, pp. 318–319.

Yusuf, M., Millas, A. L. G., Estandarte, A. K. C., Bhella, G. K., McKean, R., Bittencourt, E. & Robinson, I. K. (2014). *Biotechniques*, **57**, 137–141.

Zehbe, R., Schmitt, V. H., Kirkpatrick, C. J. & Brochhausen, C. (2014). *Mater. Sci. Technol.* **31**, 167–173.

Zhang, S. (2008). *Adv. Cancer Res.* **99**, 335–362.